SUPPORTING INFORMATION

Ferroelectric control of the spin texture in GeTe

Christian Rinaldi[1,2*], Sara Varotto[1], Marco Asa[1], Jagoda Sławińska[3], Jun Fujii[4], Giovanni Vinai[4], Stefano Cecchi[5], Domenico Di Sante[3,6], Raffaella Calarco[5], Ivana Vobornik[4], Giancarlo Panaccione[4], Silvia Picozzi[3], Riccardo Bertacco[1,2*]

[1]Department of Physics, Politecnico di Milano, 20133 Milano, Italy.

[2]IFN-CNR, c/o Politecnico di Milano, 20133 Milano, Italy.

[3]Consiglio Nazionale delle Ricerche CNR-SPIN, Sede Temporanea di Chieti, c/o Univ. "G. D'Annunzio", 66100 Chieti, Italy

[4]CNR-IOM, Laboratorio TASC in Area Science Park - Basovizza, 34149 Trieste, Italy.

[5]Paul-Drude-Institut für Festkörperelektronik, Hausvogteiplatz 5-7, 10117 Berlin, Germany

[6]Institut für Theoretische Physik und Astrophysik, Universitat Würzburg, Am Hubland Campus Süd, Würzburg 97074, Germany

*Correspondence to:

christian.rinaldi@polimi.it

Phone: +39 02 2399 9663

riccardo.bertacco@polimi.it

Phone: +39 02 2399 9661

1 Methods

1.1 Sample growth

GeTe films were epitaxially grown by MBE on Si(111) substrates (p-type B-doped, resistivity1–10 Ω cm, miscut < 0.1 degrees, 100 nm thermal oxide capping layer).[1] The substrates were wet cleaned before loading them into the MBE system and thermal desorption of water was induced in the growth chamber by annealing. An appropriate treatment allows to obtain a Si(111)-($\sqrt{3}\times\sqrt{3}$)R30°-Sb surface[2] before cooling down to the deposition temperature at 250 °C. The deposition was performed using Ge and Te dual-filament effusion cells. A Te/Ge flux ratio of ~1.6 was used. After deposition of 23 nm of GeTe, a 20 nm thick capping layer of amorphous Te was deposited on top, in order to prevent contamination upon exposure to atmosphere. To prepare a clean and well-ordered GeTe(111) surface, a controlled thermal desorption process in UHV was optimized. As detailed in section 2, a Te-rich (Ge-rich) surface with pristine polarization P_{out} (P_{in}) is obtained upon annealing at 240 °C (260 °C).

1.2 DFT calculations

Our DFT calculations were performed by using the GREEN code[3] interfaced with the SIESTA package.[4] The exchange and correlation terms were considered within the GGA in the Perdew–Burke–Ernzerhof formalism.[5] Core electrons were replaced by norm-conserving pseudopotentials of the Troulliers-Martin type. The atomic orbital (AO) basis set consisted of double-zeta polarized numerical orbitals strictly localized. The confinement energy in the basis generation process was set to 100 meV. Real space three-center integrals were computed over 3D-grids with a resolution equivalent to 1000 Rydbergs mesh cut-off. Spin–orbit coupling has been self-consistently taken into account as implemented in Ref. 6. Surface slab models were constructed as five hexagonal unit cells of α-GeTe, stacked along the [0001] direction with an additional Te (Ge) layer to simulate two unrelaxed Te- (Ge-) terminated surfaces (31 atoms in the unit cell) with different orientation of polarization (outwards and inwards). For all calculations, Brillouin zone (BZ) integrations were

performed over *k*-supercells of (20×20) while the temperature k_BT in the Fermi–Dirac distribution was set to 10 meV. Dipole-dipole interactions among the neighboring supercells were suppressed via the usual dipole corrections applied along the *z*-direction. The electronic and spin structures have been calculated in the form (**k**, *E*)-resolved projected density of states PDOS and *k*-resolved spin polarization vector **m** (*k*-resolved magnetization) employing the Green's functions matching technique described in details elsewhere.[7]

1.3 Angular resolved photoemission spectroscopy

ARPES and spin polarized ARPES (S-ARPES) spectra have been measured at the low energy branch of APE-NFFA beamline of Electra, using the Omicron-Scienta DA30 electron energy analyser that operates in the deflection mode. The beamline provides the photons in the VUV range with variable polarization; the data presented in the manuscript were acquired with the linearly polarized photons with the polarization vector lying in the scattering plane. The analyser is further equipped with two highly efficient spin polarimeters,[8] for the determination of spin polarization vector. The polarimetry is based on the low energy electron scattering from the magnetic Fe(001)-p(1x1) target,[9,10] whose magnetization can be reversed along the two easy orthogonal directions for the determination of three-dimensional spin polarization. The spin asymmetry of this scattering is 25%, equivalent to the Sherman function of Mott polarimeters. This value was used to renormalize spectra and obtain the spin polarization of photoelectrons. The energy and angular resolution without (with) spin analysis were 40 meV (100 meV) and <0.2° (<1.5°). All measurements have been performed at liquid nitrogen temperature.

1.4 Piezoresponse Force Microscopy (PFM)

Piezoresponse Force Microscopy was done using a Keysight 5600LS atomic force microscope operating in single-frequency excitation mode. Spectroscopy and imaging were performed using conductive tips by Applied NanoStructures Inc. (AppNano ANSCM-PT, highly n-doped single

crystal Si coated with Pt, L= 225 μm, k= 3 N/m). The typical AC driving amplitude was 2 V and the driving frequencies were between 20 or 250 kHz depending on the specific frequency response.

Due to the tiny piezoelectric coefficient d_{33} in GeTe (~1 pm/V[11] to be compared with ~300 pm/V for PZT[12]), and in order to measure ferroelectric hysteresis loops, we employed a two-steps PFM technique called Switching Spectroscopy (SS-PFM),[13] or Pulsed DC Mode.[14] In this mode: (i) the desired DC voltage for sample poling is applied for a given period and subsequently released; (ii) the piezoelectric response signal is measured at zero dc bias using a relatively small AC voltage. Thus, in Switching Spectroscopy the cantilever-sample electrostatic forces are unchanged during the measurements and the PFM signal mainly depends on the remanent piezoelectric deformation of the film induced by the application of DC voltage pulses. Thanks to the minimization of electrostatic effects, SS-PFM enables measurements on materials with a relatively small piezoelectric response, thus avoiding artifacts related to resonance-enhanced PFM.[15]

Finally, the uniformity of samples was checked by acquiring the hysteresis loop on many locations (~10-100 points) over the whole sample surface.

2 Engineering of Te- and Ge-rich GeTe(111) surfaces with opposite polarization

A method for preparing GeTe(111) samples with Te-rich or Ge-rich surfaces, corresponding to uniform outward and inward polarization, has been first developed and then used both for the in-situ preparation of samples S_{Te} and S_{Ge} used for the S-ARPES experiments at the APE beamline and the patterning of spin textures, like the Rashba barrier of Figure 5 in the main text. The inwards or outwards pristine ferroelectric polarization state has been obtained by using a proper thermal annealing of Te-capped GeTe//Si samples. This surface-engineering method was optimized on campus in an ultrahigh vacuum cluster system[16] equipped with electron spectroscopy tools such as Low Energy Electron Diffraction (LEED) and X-ray Photoemission Spectroscopy (XPS).

The impact of the annealing on GeTe quality and stoichiometry was already studied by some of us[17] for GeTe samples capped with silicon nitride. In that case, we showed the tendency of Te to desorb from GeTe at high temperatures, narrowing the annealing temperature range (~240-260 °C) for which a stoichiometric $Ge_{50}Te_{50}$ and an ordered (111) surface can be restored.

The recipe is similar for Te-capped samples. After insertion in the UHV chamber, an in-situ mild sputtering with Ar^+ ions removes the oxidized topmost part of the Te capping layer (see section 3 below), in order to avoid the diffusion of oxygen towards GeTe during the subsequent heating. The residual metallic Te capping layer is then desorbed by annealing at 240-260 °C, monitoring the evolution of the surface order by LEED. The stoichiometry of samples is checked afterwards by XPS using an Al-Kα X-ray source.

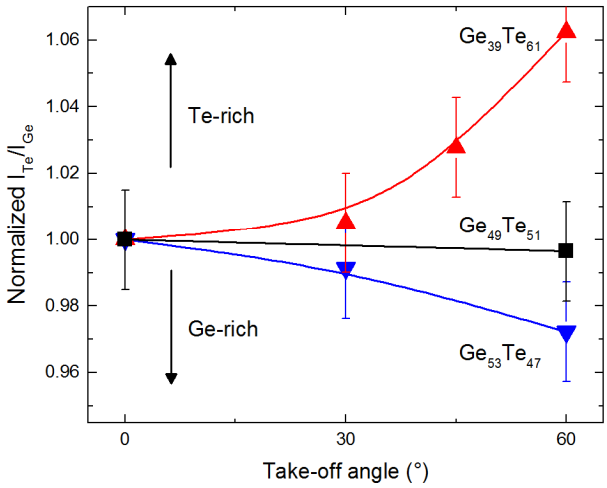

Figure S1. X-ray photoemission spectroscopy for three Te-capped GeTe sample re-prepared with different thermal budgets. The ratio between normalized Te 4d and Ge 3d peaks intensities (normalized to their cross section and analyser transmission) is reported versus the photoelectron take-off angle θ from the surface normal. The ratio I_{Te4d}/I_{Ge3d} for each angle is also normalized to their ratio at $\theta = 0$ to emphasise relative changes of this quantity. The average stoichiometry of each sample is calculated from data collected at $\theta = 0$.

Figure S1 shows the ratio between Te 4d and Ge 3d peak areas (normalized to their cross sections, transmission of the analyser and escape depth) versus the photoemission collection angle θ, for three GeTe(111) samples re-prepared with different thermal budgets. Note that the sensitivity to the surface composition increases with the take-off angle. A low thermal budget (e.g. T= 240 °C for 1 hour) is

enough to recover a hexagonal LEED pattern, associated to Te-rich GeTe(111) surface, with average stoichiometry $Ge_{39\pm2}Te_{61\pm2}$. Correspondingly, the Te 4d/Ge 3d intensity ratio increases at high collection angles, as shown by the red solid line in Figure S1. An annealing at T= 250 °C for 1 hour produces a more stoichiometric sample, with average stoichiometry $Ge_{49\pm2}Te_{51\pm2}$, displaying an almost flat behaviour of the Te 4d/Ge 3d intensity ratio versus collection angle (solid black line in Figure S1). A higher thermal budget (T= 260 °C for 1 hour) results in a Ge-rich surface ($Ge_{53\pm1}Te_{47\pm1}$), showing a surface Ge enrichment as the Te 4d/Ge 3d intensity ratio decreases with θ (solid blue line in Figure S1).

Data in Figure S1 demonstrate the possibility to act on the surface composition of GeTe(111) samples via controlled desorption of the Te capping layer. We used this calibration for the engineering of the surface stoichiometry and related pristine ferroelectric state in samples S_{Te} and S_{Ge} used for S-ARPES experiments, as described in the main text.

In order to determine the pristine ferroelectric polarization of Ge-rich and Te-rich GeTe(111) surfaces, we performed a statistical analysis of the ferroelectric polarization by ex-situ Piezoresponse Force Microscopy (PFM), immediately after exposure of samples to the atmosphere.

PFM was performed using a Keysight 5600LS atomic force microscope (AFM), operated as described in section 1.4. We recorded by Switching Spectroscopy PFM the virgin polarization curve (from zero to positive or negative bias) and the complete hysteresis loop to determine the pristine polarization state at a given point (see Figure 1c-c' in the main text and the related discussion). We repeated this analysis over a mesh of points covering the whole sample area to verify the uniformity of pristine polarization, whose distribution is reported in Figure S2 for the Te-rich ($Ge_{39}Te_{61}$) and Ge-rich ($Ge_{53}Te_{47}$) samples. Red (blue) areas correspond to a FE polarization outwards (inwards). Grey squares indicate areas with indefinite pristine polarization. Despite the presence of few domains with opposite polarization, the Te-rich sample shows a clear tendency to display outwards polarization, while for the Ge-rich sample the polarization is mainly inwards. Note that the residual domains with

opposite polarization are most probably due to some local non-uniformity in the sample heating procedure, which could be easily fixed by further optimizing the process.

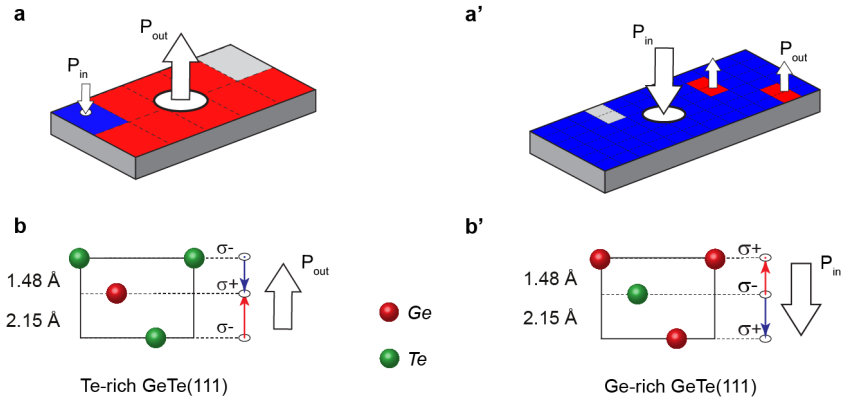

Figure S2. Statistical analysis of ferroelectricity. a, a' PFM pristine polarization map for the Te-rich ($Ge_{39\pm2}Te_{61\pm2}$) and Ge-rich ($Ge_{53\pm2}Te_{47\pm2}$) surfaces. **b, b'** Origin of the outward and inward polarizations.

To confirm the orientation of the pristine polarization and to test the stability of saturation states over time, we also investigated the evolution of ferroelectric domains written by rastering the same re-prepared sample surface with a biased AFM tip. Figure S3 shows the vertical (out-of-plane) PFM phase contrast for the Te-rich sample immediately after domain writing (panel a) and after one day (panel b). The picture frame visible in both panels was obtained by scanning over the outer 1.5 μm square with a positive tip bias, and subsequently over the inner 0.5 μm square with a negatively biased tip. The external unpoled area shows the same PFM contrast of the inner part, confirming the outward pristine polarization reported in Figure S2a. Moreover, the stability of ferroelectric domains is confirmed by the comparison of panels S3a and S3b (at least over 24 hours).

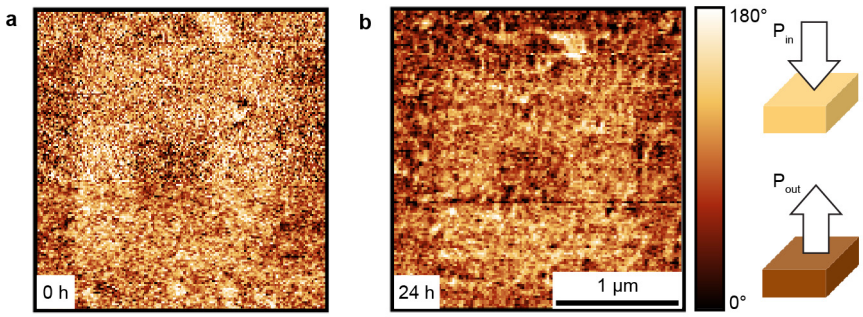

Figure S3. Ferroelectric domain stability in GeTe. Piezoresponse phase images recorded on the Te-rich sample (S_{Te}) after poling with the tip at +5 V and -5 V over 1.5×1.5 μm^2 and 0.5×0.5 μm^2 squares. The images were collected over 2.5×2.5 μm^2 areas immediately after domain writing (**a**) and 24 hours later (**b**).

Our results demonstrate the robustness and reliability of the surface-engineering approach adopted in this work to prepare GeTe(111) films with opposite and stable ferroelectric polarization, suitable as starting point for the patterning of spin textures but also for ARPES investigation. In the latter case, our approach allows to study GeTe surfaces with opposite FE polarization avoiding the very challenging in-situ switching of the polarization by electrical pulses.

3 XPS characterization of samples S_{Te} and S_{Ge}

The recipe optimized on-campus was applied at the beamline to produce clean and well-ordered α-GeTe(111) surfaces suitable for ARPES investigation. After insertion of Te-capped films in the UHV chamber, a mild sputtering by Ar^+ ions was used to remove the oxidized topmost part of the Te capping layer, in order to avoid oxygen interdiffusion in the GeTe film upon heating. The cleanness of the obtained surface can be appreciated by looking at the XPS spectra reported in Figure S4, showing a negligible trace of contaminants (C 1s and O 1s peaks).

A subsequent annealing was performed to completely decap samples, leaving a fresh GeTe surface.

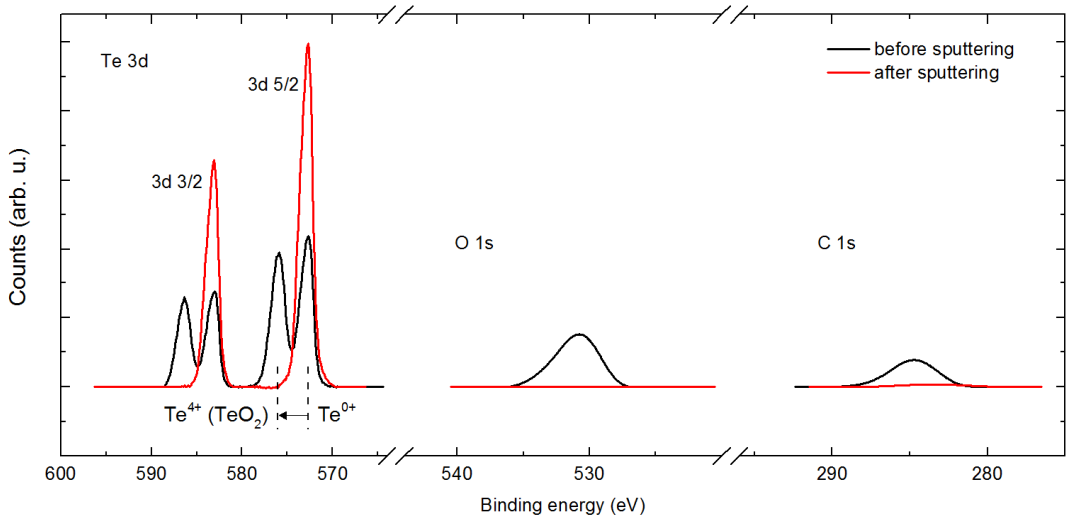

Figure S4. Removal of contaminants from the Te capping layer. XPS spectrum showing the effectiveness of the cleaning procedure. Before sputtering, the Te 3d peak is composed by two doublets, associated to Te^{0+} (metallic) and Te^{4+}oxidation states. The chemical shift between metallic and oxidized peaks is 3.2 eV, as expected for TeO_2.[18] Sputtering is able to remove oxygen from the capping layer, as evident from the disappearance of the chemically shifted Te 3d component, and O 1s peak. Even the carbon intensity (C 1s) becomes negligible.

After Te desorption we investigated the surface stoichiometry by XPS. Spectra for the determination of the surface stoichiometry reported in the main text have been taken at 800 eV photon energy, in the region of Ge 3d and Te 4d peaks. Figure S4 shows the comparison between spectra collected on S_{Te} and S_{Ge} at normal emission, immediately after desorption of the Te capping layer, when both samples displayed a hexagonal LEED pattern.

The average surface stoichiometries reported in the main text, have been retrieved by assuming a uniform distribution of Ge and Te atoms in the sample. For the cross section at 800 eV BE we used values calculated in the dipole length approximation from J. J. Yeh and I. Lindau:[19] σ_{Te}= 0.1465 and σ_{Te}= 0.2143 Mbarn, corrected for the asymmetry parameters of the subshells and the peculiar experimental geometry. The analyzer transmission T was assumed proportional to the square root of the kinetic energy. For the escape depth values of Ge 3d and Te 4d we used λ_{Ge}= 17.84 Å and λ_{Te}= 17.62 Å, as calculated by the NIST Electron Effective-Attenuation-Length Database software[20] for GeTe.

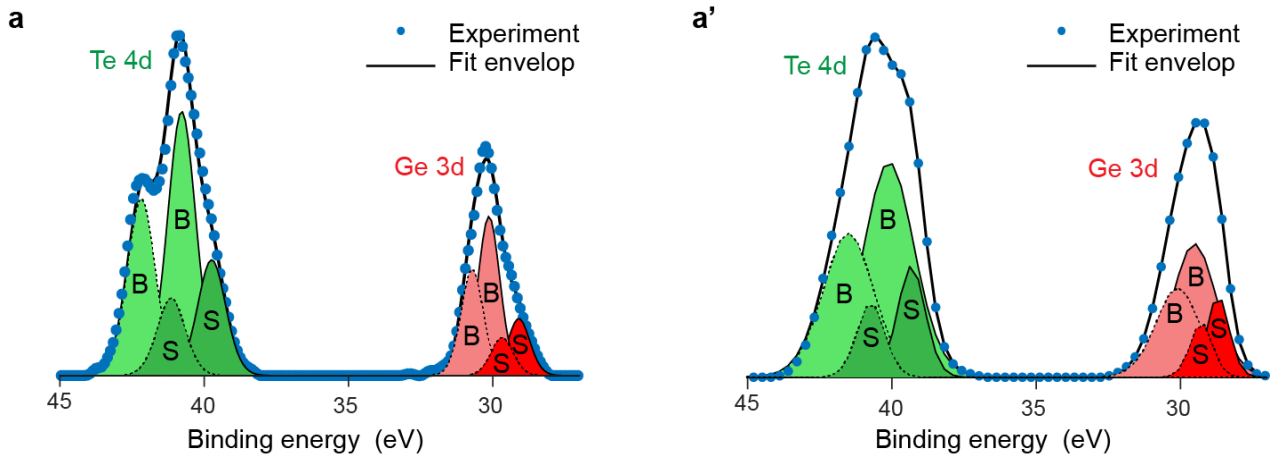

Figure S5. X-ray photoemission spectra taken at 800 eV photon energy. a, a' Ge 3d and Te 4d peaks for S_{Te} and S_{Ge} samples, respectively (after Shirley background subtraction).

The average stoichiometries obtained in this way are $Ge_{0.39}Te_{0.61}$ for S_{Te} and $Ge_{0.46}Te_{0.54}$ for S_{Ge}. As discussed in the main text, the average stoichiometries reported above should not be compared with the ideal $Ge_{0.5}Te_{0.5}$, but with the composition of real films typically affected by 10% Ge vacancies,

i.e. $Ge_{0.45}Te_{0.55}$.[21] The difference of the average stoichiometry is well above the relative error bar (2%), thus indicating that S_{Te} is definitely Te-rich while S_{Ge} appears slightly Ge-rich, even though the deviation from the assumed "nominal" Ge-deficient concentration is within our error bar.

The same samples have been analyzed by XPS after the beamtime, in the apparatus used for the optimization of the surface engineering strategy. The stoichiometries obtained at 1486.6 eV photon energy, $Ge_{0.38}Te_{0.62}$ for S_{Te} and $Ge_{0.61}Te_{0.39}$ for S_{Ge}, are different from those at 800 eV, most probably due to the uncertainty on the cross sections, but clearly confirm that S_{Te} and S_{Ge} are Te-rich and Ge-rich, respectively. Furthermore, according to the calibration of our recipe presented above, S_{Te} (S_{Ge}) displays a uniform pristine outward (inward) polarization.

	Sample S_{Te}			**Sample S_{Ge}**		
Peak	**BE (eV)**	**FWHM**	**Area/σ**	**BE (eV)**	**FWHM**	**Area/σ**
Te $4d_{5/2}$ S	39.74	1.14	1.30	39.30	1.12	0.33
Te $4d_{3/2}$ S	41.14	1.14	0.88	40.70	1.12	0.22
Te $4d_{5/2}$ B	40.78	1.14	2.99	40.08	2.06	1.18
Te $4d_{3/2}$ B	42.18	1.14	2.00	41.48	2.06	0.79
Ge $3d_{5/2}$ S	29.10	0.90	0.74	28.69	0.90	0.2
Ge $3d_{3/2}$ S	29.68	0.90	0.53	29.27	0.90	0.13
Ge $3d_{5/2}$ B	30.13	0.90	2.11	29,51	1.78	0.63
Ge $3d_{3/2}$ B	30.71	0.90	1.42	30,09	1.78	0.42

Table S1. Parameters used for fitting XPS spectra from S_{Te} and S_{Ge} reported in Figure S5. The peak areas have been normalized to the cross sections (σ) reported in the text and analyzer transmission. The suffix "S" refers to surface features, while "B" refers to bulk ones.

Further insights on the surface and bulk stoichiometry come from the deconvolution of the Ge 3d and Te 4d peaks reported in Figure S5. In order to obtain a good fit, we used two doublets for each peak,

with the nominal branching ratio and spin-orbit splitting. The situation appears different form that reported by L. Yashina *et al.*,[22] as in our case the surface present negligible oxidation.

Doublets at higher binding energy (BE) are attributed to bulk, while those at lower BE to surface, as arising from the lower atomic coordination and final state effects. This decomposition is confirmed by spectra collected with enhanced surface sensitivity (i.e. at 445 eV photon energy, data not shown), showing an increase of the lower BE component related to surface. From the comparison of the two spectra of Figure S5, peaks of S_{Ge} apppear much broader. We correlate this fact to the larger downwards band bending expected in a Ge-terminated surface, which does not display surface states and thus has a reduced capability of pinning the Fermi level at surface. Based on this we used a fixed linewidth for surface components and a variable one for the bulk, as the energy broadening associated to band bending is supposed to affect only the bulk components. The parameters of the fit are reported in Table S1. Looking at the surface and bulk stoichiometries that can be extracted from the normalized peak areas in Table S1, we find the situation summarized in Table S2.

We obtain a surface stoichiometry Te-rich in S_{Te} and Ge-rich in S_{Ge}, while the values of the bulk stoichiometry found for the two samples are almost identical, within the uncertainty of at least ±0.05 which arises from the fitting. This analysis clearly points to the presence of a surface layer more Te (Ge) rich in the two samples, which could be associated to different terminations, as expected for GeTe surfaces with opposite pristine ferroelectric polarizations.

Sample	**Surface stoichiometry** (± 0.05)	**Bulk stoichiometry** (± 0.05)
S_{Te}	$Ge_{0.37}Te_{0.63}$	$Ge_{0.41}Te_{0.59}$
S_{Ge}	$Ge_{0.47}Te_{0.53}$	$Ge_{0.44}Te_{0.56}$

Table S2. Surface and bulk stoichiometry for the two samples as derived from the intensity of the surface and bulk peaks used in the fitting of Figure S5.

4 Vectorial analysis of the spin texture

The APE Low Energy end station at the Elettra synchrotron radiation facility is equipped with the Omicron-Scienta DA30 electron energy analyser followed by two VLEED polarimeters, as described in the Methods of the main text. One VLEED measures the spin asymmetry along the direction parallel to the k_x axis (in the plane) and the k_z axis (out of plane) of the sample, while the other is designed to measure along the k_y direction and along k_z too. The combined use of the two detectors allows to reconstruct the spatial orientation of photoelectrons' spins, as reported in Figure S6. Panels c' and d' show the spin polarized spectra and the non-negligible spin polarization projected along k_x (ZA), and are the same as in Figure 4b' and 4c' of the main text. On the contrary, panels e' and f' show the absence of spin polarization along k_y (ZU). The same holds for the out-of-plane spin component reported in panels g' and h'. The vectorial analysis confirms that the in-plane spin component is orthogonal to the wave vector, as expected for the linear term of the Rashba Hamiltonian. The absence of out-of-plane component agrees with the calculations along ZU for the cubic Rashba term.[23]

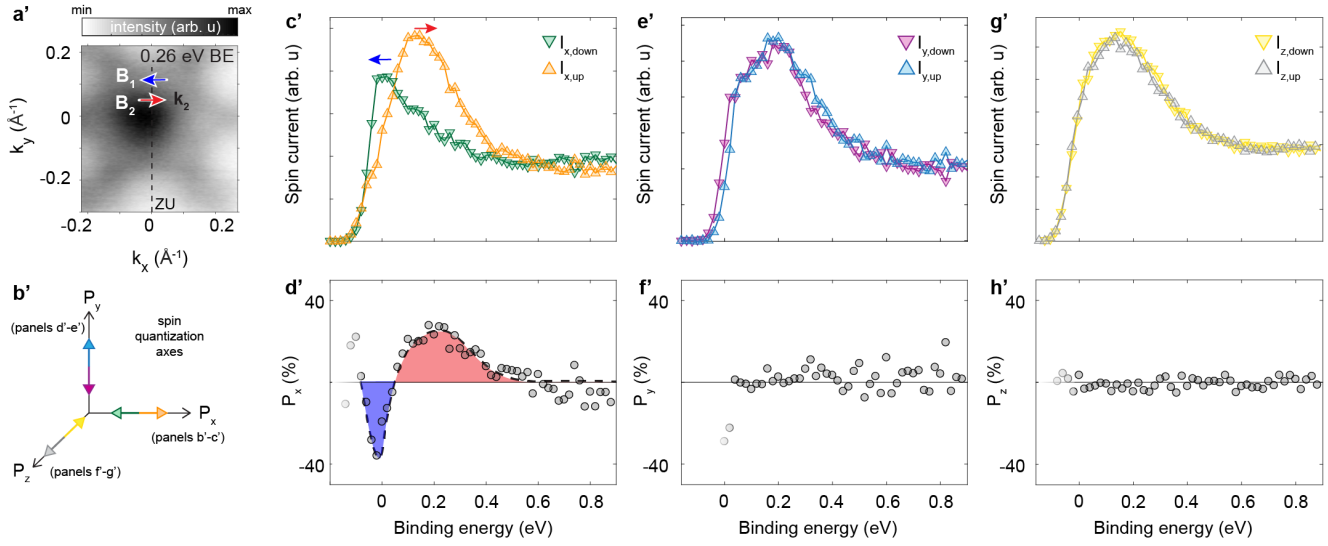

Figure S6. Vectorial analysis of the spin in S_{Ge}. a' Constant energy map at 0.26 eV BE. $\mathbf{k_2}$ is the wave vector where spin spectra have been collected. **b'** Complete reference frame for the spin obtained by the combined use of the two VLEED. The spin currents and resulting spin polarization are reported in panels **c'-d'** for the *x*, **e'-f'** for the *y* and **g'-h'** for the *z* quantization axes.

5 DFT calculations of GeTe(111) surfaces with unstable terminations

For the sake of completeness, in Figure S7 we show the spectral function also for unstable cases (i.e. Ge-terminated with outwards polarization and Te-terminated for inwards polarization).[24]

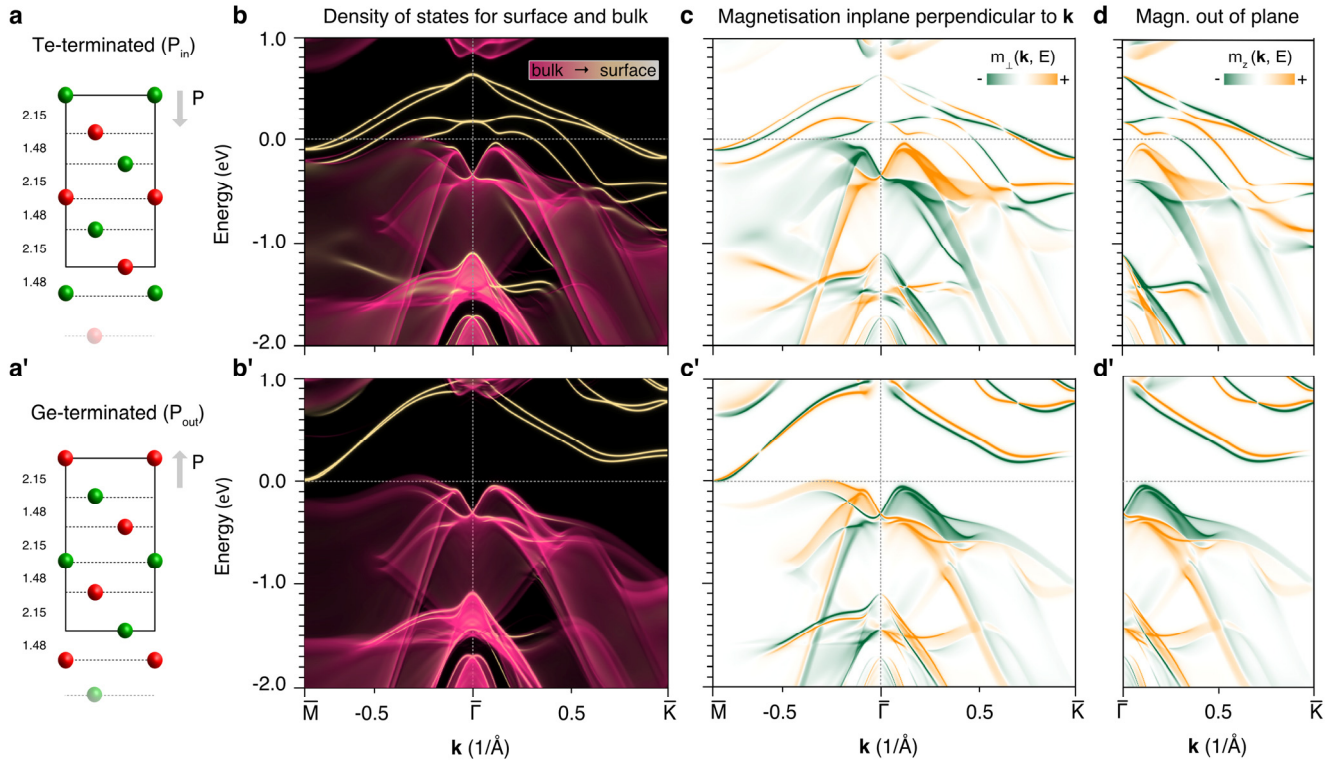

Figure S7. DFT calculations of GeTe(111) surfaces with unstable terminations. a Side view of Te-terminated surface with polarization inwards. Green (red) balls denote Te (Ge) atoms; only the topmost layers of the slab are shown. The numbers on the left indicate the unrelaxed interlayer distances given in Å. **b** Density of states at Te-terminated GeTe(111) surface shown in **a**, projected on surface (pink) and bulk (yellow) principal layers calculated via Green's functions technique for the semi-infinite model of the surface. Brighter tones of pink (yellow) bands indicate higher intensity of bulk (surface) features. Both high-symmetry directions are defined in Figure 2d in the main text. **c** Density of magnetization vector along high symmetry directions. Only in-plane components perpendicular to the momentum are shown, since the components parallel to **k** vanish within the whole BZ. **d** Out-of-plane magnetization density component calculated along $\overline{\Gamma K}$; along the $\overline{\Gamma M}$ line $m_z = 0$. **a'-d'** Same as a-d for Ge-terminated surface, with polarization outwards. The Fermi level has been shifted in order to align the bulk bands of Te- and Ge-terminated surfaces. In **d'** the line $\overline{\Gamma M}$ is not shown, but it has to be noted that the surface states in the unoccupied part of the spectrum reveal some non-negligible traces of m_z along this direction.

References

(1) Wang, R.; Boschker, J. E.; Bruyer, E.; Sante, D. Di; Picozzi, S.; Perumal, K.; Giussani, A.; Riechert, H.; Calarco, R. *J. Phys. Chem. C* **2014**, *118* (51), 29724–29730.

(2) Boschker, J. E.; Momand, J.; Bragaglia, V.; Wang, R.; Perumal, K.; Giussani, A.; Kooi, B. J.; Riechert, H.; Calarco, R. *Nano Lett.* **2014**, *14* (6), 3534–3538.

(3) Cerdá, J., Van Hove, M. A., Sautet, P. & Salmeron, M. *Phys. Rev. B* **1997**, *56*, 15885–15899.

(4) Soler, J. M.; Artacho, E.; Gale, J. D.; García, A.; Junquera, J.; Ordejón, P.; Sánchez-Portal, D. *J. Phys. Condens. Matter* **2002**, *14* (11), 2745–2779.

(5) Perdew, J. P., Burke, K. & Ernzerhof, M. *Phys. Rev. Lett.* **1996**, *77*, 3865–3868.

(6) Cuadrado, R. & Cerdá, J. *J. Phys. Condens. Matter* **2012**, *24*, 86005.

(7) Rossen, E. T. R., Flipse, C. F. J. & Cerdá, J. I. *Phys. Rev. B* **2013**, *87*, 235412.

(8) Bigi, C.; Das, P. K.; Benedetti, D.; Salvador, F.; Krizmancic, D.; Sergo, R.; Martin, A.; Panaccione, G.; Rossi, G.; Fujii, J.; Vobornik, I. *J. Synchrotron Radiat.* **2017**, *24* (4), 750–756.

(9) Bertacco, R.; Onofrio, D.; Ciccacci, F. *Rev. Sci. Instrum.* **1999**, *70* (9), 3572–3576.

(10) Bertacco, R.; Marcon, M.; Trezzi, G.; Duò, L.; Ciccacci, F. *Rev. Sci. Instrum.* **2002**, *73* (11), 3867.

(11) Gervacio-Arciniega, J. J.; Prokhorov, E.; Espinoza-Beltrán, F. J.; Trapaga, G. *J. Appl. Phys.* **2012**, *112* (5), 52018.

(12) Alexe, M.; Gruverman, A. *Nanoscale Characterisation of Ferroelectric Materials: Scanning Probe Microscopy Approach*; NanoScience and Technology; Springer Berlin Heidelberg, 2013.

(13) Jesse, S.; Baddorf, A. P.; Kalinin, S. V. *Appl. Phys. Lett.* **2006**, *88* (6), 62908.

(14) Hong, S.; Woo, J.; Shin, H.; Jeon, J. U.; Pak, Y. E.; Colla, E. L.; Setter, N.; Kim, E.; No, K. *J. Appl. Phys.* **2001**, *89* (2), 1377–1386.

(15) Kolobov, A. V; Kim, D. J.; Giussani, A.; Fons, P.; Tominaga, J.; Calarco, R.; Gruverman, A. *APL Mater.* **2014**, *2* (6), 66101.

(16) Bertacco, R.; Cantoni, M.; Riva, M.; Tagliaferri, A.; Ciccacci, F. *Appl. Surf. Sci.* **2005**, *252* (5), 1754–1764.

(17) Rinaldi, C.; Rojas-Sánchez, J. C.; Wang, R. N.; Fu, Y.; Oyarzun, S.; Vila, L.; Bertoli, S.; Asa, M.; Baldrati, L.; Cantoni, M.; George, J. M.; Calarco, R.; Fert, A.; Bertacco, R. *APL Mater.* **2016**, *4* (3), 32501.

(18) Christie, A. B.; Sutherland, I.; Walls, J. M. *Surf. Sci.* **1983**, *135* (1), 225–242.

(19) Yeh, J. J.; Lindau, I. *At. Data Nucl. Data Tables* **1985**, *32* (1), 1–155.

(20) U.S. National Institute of Standards and Technology (NIST). Standard Reference Database 82 (Electron Effective-Attenuation-Length) available at https://www.nist.gov/srd/nist-standard-reference-database-82.

(21) Perumal, K. Epitaxial Growth of Ge-Sb-Te based Phase Change Materials, Humboldt-Universität zu Berlin, 2013.

(22) Yashina, L. V; Püttner, R.; Neudachina, V. S.; Zyubina, T. S.; Shtanov, V. I.; Poygin, M. V. *J. Appl. Phys.* **2008**, *103* (9), 94909.

(23) Di Sante, D.; Barone, P.; Bertacco, R.; Picozzi, S. *Adv. Mater.* **2012**, *25* (4), 509–513.

(24) Deringer, V. L.; Lumeij, M.; Dronskowski, R. *J. Phys. Chem. C* **2012**, *116* (29), 15801–15811.